Journal of Structural Biology 177 (2012) 202–211

Contents lists available at SciVerse ScienceDirect

Journal of Structural Biology

journal homepage: www.elsevier.com/locate/yjsbi

# Cryo X-ray nano-tomography of vaccinia virus infected cells

Francisco Javier Chichón [a,1], Maria Josefa Rodríguez [a,1], Eva Pereiro [b], Michele Chiappi [a], Beatriz Perdiguero [a], Peter Guttmann [c], Stephan Werner [c], Stefan Rehbein [c], Gerd Schneider [c], Mariano Esteban [a], José L. Carrascosa [a,d,*]

[a] Centro Nacional de Biotecnología-Consejo Superior de Investigaciones Científicas (CNB-CSIC), Campus Cantoblanco, 28049 Madrid, Spain
[b] ALBA Synchrotron Light Source, MISTRAL Beamline – Experiments Division, 08290 Cerdanyola del Vallès, Barcelona, Spain
[c] Helmholtz-Zentrum Berlin für Materialien und Energie GmbH, Institute Soft Matters and Functional Materials, Electron Storage Ring BESSY II, Albert-Einstein-Str. 15, 12489 Berlin, Germany
[d] Instituto Madrileño de Estudios Avanzados en Nanociencia (IMDEA Nanociencia) Cantoblanco, Madrid, Spain

ARTICLE INFO

*Article history:*
Available online 8 December 2011

*Keywords:*
Cryo X-ray nano-tomography
Electron tomography
Correlative microscopy
Vaccinia virus
Virus assembly
Radiation damage

ABSTRACT

We have performed full-field cryo X-ray microscopy in the water window photon energy range on vaccinia virus (VACV) infected cells to produce tomographic reconstructions. PtK2 cells were infected with a GFP-expressing VACV strain and frozen by plunge fast freezing. The infected cells were selected by light fluorescence microscopy of the GFP marker and subsequently imaged in the X-ray microscope under cryogenic conditions. Tomographic tilt series of X-ray images were used to yield three-dimensional reconstructions showing different cell organelles (nuclei, mitochondria, filaments), together with other structures derived from the virus infection. Among them, it was possible to detect viral factories and two types of viral particles related to different maturation steps of VACV (immature and mature particles), which were compared to images obtained by standard electron microscopy of the same type of cells. In addition, the effect of radiation damage during X-ray tomographic acquisition was analyzed. Thin sections studied by electron microscopy revealed that the morphological features of the cells do not present noticeable changes after irradiation. Our findings show that cryo X-ray nano-tomography is a powerful tool for collecting three-dimensional structural information from frozen, unfixed, unstained whole cells with sufficient resolution to detect different virus particles exhibiting distinct maturation levels.



## 1. Introduction

The process of virus infection of eukaryotic cells is a classical example on how the coupling in the host cell of the assembly of viral structural components to their spatial and temporal organization leads to efficient production of progeny. Viral components are produced under a temporal control, and they are subsequently transported to the proper assembly sites using cellular pathways. These areas define assembly factories where the concentration and access of viral components are optimized. During these steps there are extensive interactions between viral and cellular components that have been studied for decades as a main target to design antiviral strategies, as well as an attractive model system to understand the molecular basis for cell control and macromolecular interactions. In particular, the role of cell membranes in the viral assembly has been extensively documented for many viral systems, including the involvement of endoplasmic reticulum (ER) for rotavirus, the role of ER–Golgi intermediate compartment for coronavirus and poxvirus assembly and maturation, and the plasma membrane in the production of retrovirus, orthomyxovirus and paramyxovirus, among others (reviewed in Hunter, 2007).

The study of viral life cycles involves the correlation of biochemical and structural approaches to yield the proper detailed description of the different steps of the cycle: specific recognition of the host, incorporation of the viral genome into the cell, transcription and replication of the genome, assembly of the infective virus and the final exit from the host cell (reviewed in Flint et al., 2009). While improved visible light microscopy has been widely used for whole cell structural analyses of viral infection, the increasing demand of higher resolution to get deeper insights into these processes have led to the incremental use of powerful methods, as electron cryo-tomography (Lucic et al., 2005), revealing molecular details albeit with the cost of a reduction of the complexity or scale of the sample, while increasing the sample preparation difficulty. The inherent limitation of the analysis at the cellular level (sample thicknesses about 300–500 nm for electron

* Corresponding author at: Centro Nacional de Biotecnología-Consejo Superior de Investigaciones Científicas (CNB-CSIC), Campus Cantoblanco, 28049 Madrid, Spain. Fax: +34 915854506.
*E-mail address:* jlcarras@cnb.csic.es (J.L. Carrascosa).
[1] Both authors contributed equally to this work.

1047-8477/$ - see front matter © 2011 Elsevier Inc. All rights reserved.
doi:10.1016/j.jsb.2011.12.001

microscopes), together with the consequent lack of quantification due to the sample limitations imposed by high resolution methods, have become critical problems for the correlation of these qualitative structural data with the quantitative data derived from whole populations using biochemical, genetic and proteome analyses (Baumeister and Steven, 2000; Martone et al., 2003).

There are different alternatives to overcome the resolution limits imposed either by visible light microscopy based analyses, or by the penetration power of transmission electron microscopy (TEM) to deal with thick, whole cell samples. Different super-resolution visible light fluorescence microscopy methods (Galbraith and Galbraith, 2011; Jones et al., 2011), and the use of improved sectioning methods in electron tomography (Pierson et al., 2010; Rigort et al., 2010) are opening new possibilities for the comprehensive study of the cellular cartography. The use of X-ray microscopy is another powerful alternative, based on the high penetration power of soft X-rays in the water window photon energy range (just below the O absorption K edge at 543 eV) in hydrated biological material (sample thicknesses $\leqslant$10 microns). The use of diffractive optics in full-field X-ray microscopes (Chao et al., 2005; Rehbein et al., 2009; Schneider et al., 1995), together with the incorporation of cryogenic procedures for sample preparation and data acquisition (Schneider, 1998), have led to the recent success of X-ray microscopy for 3-D imaging of cells yielding tomographic reconstructions at resolutions in the order of 20–30 nm (Hanssen et al., 2010; Larabell and Le Gros, 2003; Larabell and Nugent, 2010; Schneider et al., 2002, 2003, 2010; Weiss et al., 2000).

The estimation of the effective resolution attainable by cryo X-ray nano-tomography (cryo-X-nano-tomo) of whole cell samples is a critical parameter to evaluate its possibilities for the detailed analysis of the cartography of cellular components. A quantitative estimation for such a resolution was experimentally obtained by comparison of the tomographic reconstructions of a large and complex virus (VACV) using both X-ray and electron microscopies (Carrascosa et al., 2009). The resolution from X-ray tomograms using a zone plate of 25 nm was found to be only 3,7 times lower than that obtained from electron microscopy (*i.e.* 25.7 nm vs 6.7 nm), thus opening the possibility to resolve structural features of small cellular complexes and aggregates in whole cells at resolutions between light and electron microscopies. As those resolution estimations were done on purified virus preparations in buffer, a critical question is whether such features could be distinguished within the complex and crowded cellular media. In this work we show the possibility to detect VACV individual particles in the cytoplasm of an infected whole cell without chemical fixation, sectioning or labeling by cryo X-ray tomography with an estimated 3D-resolution up to 55 nm using a zone plate of 40 nm, which allowed fulfilling better depth of focus requirements.

Vaccinia virus (VAVC) is the best known member of the Poxviridae family. The virus particle is relatively large ($360 \times 270 \times 250\ nm^3$), enclosing a core with a double stranded DNA containing more than 200 open reading frames coding for viral specific proteins (Cyrklaff et al., 2005; Moss, 2007). The assembly of VACV is very complex, starting with the modification of cellular membranes at the ER by incorporation of viral proteins, giving rise to crescents. These modified membranes evolve to rounded immature virus particles (IV) which contain a complex viroplasm. The IVs incorporate viral DNA and they enter in a complex maturation process involving the reorganization of viral envelopes, the formation of a distinct core, and a severe change in the overall structure, yielding the characteristic brick-shaped mature virus (MV). These particles, although infective, are not the final form of the viral maturation: they are able to interact with the trans-Golgi network to produce a wrapped form of the virus (WV), which is transported towards the outer plasma membrane of the cell using a kinesin-based microtubular mechanism. Later in the infection cycle, the virus particles associate to the cell membrane and are further ejected from the cells using actin polymerization to efficiently spread the virus along large microvilli (reviewed in Flint et al., 2009; Moss, 2007).

The maturation process of VACV is carried out entirely in the cell cytoplasm, and it involves multiple sets of temporal interactions between cellular membranes and other organelles with viral components. Due to the complexity of these interactions, their study has been difficult and several controversies related to the total number of viral membranes and their cellular origin are still open (reviewed in Rodriguez et al., 2006). Part of these problems are derived from the fact that most of the studies were based on the very limited and partial information that is retrieved from ultra-thin sections of 50–100 nm from a total cell thickness of 10–20 μm or more. Furthermore, the electron microscope images from those sections overlap their structural features in two-dimensional projections, thus leading to conflicting interpretations. The use of electron tomography was a main step towards the understanding of the virus structure (Cyrklaff et al., 2005), assembly (Chichon et al., 2009) and disassembly (Cyrklaff et al., 2007). Tomographic reconstructions reveal genuine three-dimensional information, thus avoiding the superposition of information found in projected images. Nevertheless, even in these cases the information is retrieved from a small percentage of the volume of the whole cell, thus preventing the quantitative analysis of the viral life cycle at the cellular level. In an attempt to circumvent these problems, we have explored the combination of fast freezing of VACV infected cells with X-ray microscopy to get insights into the viral infection process at the whole cell level taking profit of the penetration power of X-rays. The VACV structural knowledge obtained by the analysis of the same cell type by standard electron microscopy approaches allowed us to identify the viral related structures within the X-ray tomograms. Our results demonstrate that it is possible to detect different types of viral assembly intermediates within the cytoplasm of whole cells. In addition, we studied the effect of radiation damage by TEM analysis of plastic embedded thin sections of X-ray irradiated cells. The results revealed no noticeable changes in the cellular ultrastructure during the tomographic data acquisition by X-ray microscopy.

## 2. Materials and methods

### 2.1. Cells and viruses

The established chick embryo cell line DF-1 and PtK2 cells were grown in Dulbecco's modified Eagle's medium (DMEM) supplemented with 10% fetal calf serum (FCS). Cells were maintained in a humidified air 5% $CO_2$ atmosphere at 37 °C. Virus infections were performed with 2% FCS for both cell types. The VACV strains used in this work include Western Reserve (WR), modified vaccinia virus Ankara (MVA) obtained from the Ankara strain after 586 serial passages in primary chick embryo fibroblast cells (CEF) (derived from clone F6 at passage 585, kindly provided by G. Sutter, Germany) and MVA-C-ΔF1L expressing from the TK locus gp120 and Gag-Pol-Nef proteins of HIV-1 (subtype C) under the transcriptional control of the synthetic early/late promoter and with the anti-apoptotic virus F1L gene replaced by rsGFP gene (Perdiguero et al., in preparation).

### 2.2. Analysis of virus growth

To determine virus growth profiles, monolayers of PtK2 cells grown in 12-well tissue culture plates were infected at 0.01 PFU/cell with WR, MVA or recombinant MVA-C-ΔF1L(GFP). Following virus adsorption for 60 min at 37 °C, the inoculum was removed,

the infected cells were washed once with DMEM without serum and incubated with fresh DMEM containing 2% FCS at 37 °C in a 5% $CO_2$ atmosphere. At different post-infection times (0, 24, 48 and 72 h), cells were removed by scraping (cell lysates at $5 \times 10^5$ cells/ml), freeze–thawed three times and briefly sonicated. Infectious viruses in cell lysates were measured by immunostaining assay in DF-1 cells.

### 2.3. Immunostaining assay

Virus titers in cell lysates were determined by immunostaining assay according to the following protocol. Grow DF-1 cells in 6-well plates to reach near confluency. Make 10-fold serial dilutions of the virus in complete DMEM and add 0.4 ml of each dilution to cells. Incubate 1 h in a $CO_2$ incubator at 37 °C, remove the inoculum and add complete DMEM+2% of NCS. At 48 h post-infection wash the 6-well plates with PBS and add 1:1 acetone/methanol for 2 min. Remove fixative and wash with PBS. Dilute rabbit polyclonal anti-vaccinia antibody (diluted 1:1000; CNB product) in PBS containing 3% FCS and add 1 ml/well. Incubate 1 h at room temperature with gentle rocking and wash three times with PBS. Dilute goat polyclonal anti-rabbit-HRP secondary antibody (SIGMA) in PBS containing 3% FCS at 1:1000 dilution and add 1 ml/well. Incubate 1 h at room temperature with gentle rocking and then wash three times with PBS. Make up diaminobenzidine (SIGMA) one tablet in 12 ml PBS. Filter the solution and just before use add 120 μl of 3% nickel sulfate and 12 μl of hydrogen peroxide (30% w/w). Add 500 μl of substrate solution to each well, rotate dish gently and let it stand approx. for 10 min. When the development is complete, wash the plate once with PBS. Count the number of stained foci and express titer as plaque forming units (PFU)/ml. A well containing between 50 and 100 spots is considered to be optimal for the calculation of the titer.

### 2.4. Sample preparation for microscopy

PtK2 cells were cultured on coverslips in DMEM (Dulbecco's modified Eagle medium) supplemented with 10% heat-inactivated FBS (fetal bovine serum), 2 mM L-glutamine (Gibco BRL, Life Technologies), 100 units of penicillin per ml and 100 μg of streptomycin per ml (Gibco BRL, Life Technologies). The cell line was grown as an adherent culture in an incubator (5% $CO_2$) at 37 °C. After removing FBS from the growth medium during at least 8 h (to induce the particular flat morphology of this cell line), the cells were infected with MVA-C-ΔF1C(GFP) strain (Perdiguero et al., in preparation), at a MOI (multiplicity of infection) of 10 PFU/cell. Following virus adsorption, cells were incubated for 60 min at 37 °C with intermittent stirring; the cells were washed with DMEM and placed in fresh DMEM serum free at 37 °C. At 18 h after infection, cell monolayers were either fast frozen by plunging in liquid ethane, or fixed. For routine fixation, cells were treated with a mixture of 2% paraformaldehyde and 2.5% glutaraldehyde in PBS (pH 7.4) for 1 h at room temperature.

Au-grids of the HZB2 type were coated with either formvar/carbon or carbon film to grow PtK2 cells. The carbon films were prepared by electron beam evaporation onto mica and were then floated onto water and picked up with bare grids or formvar-coated grids. The grids were sterilized by at least 2 h-exposure to UV light. PtK2 cells were then cultivated and infected on the grids following the same protocol as that used for coverslips. Parallel cell cultures were done on coverslips and classical plastic support (plates) for culture quality assessment.

### 2.5. X-ray microscopy

The HZB2 Carbon-Formwar or HZB2 Carbon Au-grids with the VACV infected cells were first imaged *in vivo* by visible light fluorescent microscopy in a Leica DMI6000B, and a SP5 confocal microscope with the 20X objective lenses. The samples, once imaged, were vitrified by plunge freezing in a Leica EM-CPC. The frozen grids were transferred to the HZB X-ray microscope (beamline U41 at the BESSY II electron storage ring (Berlin, Germany)) under cryogenic conditions. The GFP signal allowed us to identify infected cells after plunge freezing in the visible light fluorescent microscope (100×, NA = 0.75) which has been integrated in the HZB X-ray microscope. We used a photon energy (*i.e.* 510 eV) within the water window to take advantage of the high natural contrast of the biological material to acquire X-ray tomography data sets with the conditions described in (Carrascosa et al., 2009; Schneider et al., 2010). More than 40 datasets were acquired using a zone plate objective with an outermost zone width of $dr_n = 40$ nm, whereas a zone plate with $dr_n = 25$ nm was used for the acquisition of 4 datasets. The effective pixel sizes in the images were 15.6 nm or 8.6 nm (with the 40 nm zone plate objective, depending on the magnification), and 9.7 nm (with the 25 nm objective). The image stacks were pre-processed to normalize and correct the intensity distribution delivered to the sample by the capillary condenser using flat field images in a program developed for XMIPP3.0 software package (Marabini et al., 1996; Scheres et al., 2008; Schneider et al., 2010; Sorzano et al., 2004). Alignment of the tilted series was done with IMOD (Kremer et al., 1996), and the final reconstructions were performed using the iterative SIRT reconstruction option in TOMO3D (Agulleiro and Fernandez, 2011). To enhance the signal to noise levels we used TOMOBFLOW (Fernandez, 2009). The visualization and segmentation of the final volumes was carried out in Amira©, IMOD and Chimera (Pettersen et al., 2004). The 3D-resolution estimation was done using the same approach as in Carrascosa et al. (2009).

### 2.6. Standard embedding

For ultrastructural studies under electron microscopy, cells were cultured on coverslips and fixed *in situ* with a mixture of 2% paraformaldehyde (TAAB) and 2.5% glutaraldehyde (TAAB) (1 h at room temperature), washed with PBS and distilled water, post-fixed with 1% osmium tetroxide in PBS (45 min), washed with distilled water, treated with 1% aqueous uranyl acetate (45 min), dehydrated with growing quantities of ethanol and embedded in epoxy resin 812 (TAAB) for 2 days at room temperature. Capsules were polymerized for 2 days at 60 °C. Resin was detached from the coverslips by successive immersions in liquid nitrogen and hot water. Ultrathin, 70-nm-thick sections were cut in parallel to the monolayer, transferred to formvar-coated EM buttonhole grids and stained with aqueous uranyl acetate for 10 min and lead citrate for 3 min. Sections were visualized on a JEOL JEM 1200 EXII electron microscope (operating at 100 kV).

### 2.7. Fast freezing and freeze-substitution

For comparative studies, infected cells were fast frozen by plunge freezing and processed for embedding in the acrylic resin Lowicryl HM23. Briefly, infected cells grown on HZB2 Au-grids were mounted in a plunging device and the excess of medium was removed by blotting with Whatman Nr.1 paper at the wider part of the front side of the grids, for less than 5 s. After plunging in liquid ethane, frozen specimens were either directly stored for X-ray microscopy inspection, or they were transferred into a Reichert–Jung AFS freeze-substitution unit (Leica, Vienna, Austria) and maintained for 60 h in pure methanol and 0.5% (w/v) uranyl acetate. Samples were then subjected to a controlled increase of temperature before being embedded in HM23 and polymerized with UV light, for 2 days at −40 °C, and then by 2 additional days at room temperature (22 °C). Ultrathin (70 nm thick) sections were

obtained, transferred to formvar-coated EM buttonhole grids as described before and post-stained twice: with uranyl acetate for 10 min and lead citrate for 3 min in a first round of staining, and with aqueous uranyl acetate overnight in a second round.

### 2.8. Serial sectioning

The 70 nm serial sections of fast frozen PtK2-infected cells were obtained with the Ultracut UCT ultramicrotome (Leica Microsystems). Ribbons of 5–10 serial sections were sequentially distributed on formvar-coated EM buttonhole grids and subjected to uranyl acetate/lead citrate stain as described above. Specific cells were followed and imaged at low and high magnification, from the bottom to the top of these cells, in the whole set of serial sections.

### 2.9. Freeze-substitution and sample preparation after X-ray irradiation

The X-ray irradiated frozen samples were recovered after X-ray imaging and maintained in liquid nitrogen to be later subjected to freeze-substitution as described above. Once the capsules were polymerized, areas containing irradiated cells, as well as non-irradiated areas, were cut with a razor blade, removing the wider part of the grid. The remaining fragment was glued onto an Epoxy-resin capsule to allow mounting the fragment in the ultramicrotome. The selected irradiated and non-irradiated areas were identified due to the marks on the grid, and all the material around them was trimmed with a razor blade. In this way the cells of interest could be kept in the center of the block front. The Lowicryl HM23 excess on the surface of the grid was carefully removed with a razor blade. Usually, the rest of the metal grid was removed in this process without disturbing the surface of the block. A scheme for the workflow of this procedure is shown in Supplementary material Fig. S1. Serial ultrathin (70 nm) sections were taken as described above, but in this case they were stained only once during 10 min with aqueous uranyl acetate and 3 min with lead citrate.

## 3. Results

### 3.1. MVA-C-ΔF1C infection of PtK2 cells

PtK2 cells adopt a flat morphology after serum deprivation (Cyrklaff et al., 2007). Eight hours after serum removal, PtK2 cells present a standard aspect albeit with some vacuolization (Fig. 1a, b, d). The thickness of these flatten cells is around 3–10 μm, depending on the cellular area, thus in the order of magnitude required for efficient freezing and X-ray transmission microscopy using the water window energy range (Kirz and Rarback, 1985; Schneider, 1998). Infection of the flat PtK2 cells by MVA-C-ΔF1C(GFP) strain clearly increases vacuolization, as readily seen in visible light microscopy (Fig. 1c) and in electron microscopy of thin sections of these cells (Fig. 1e). This enhanced vacuolization is likely due to apoptotic events induced by virus infection, since the gene F1L encoding an inhibitor of apoptosis was deleted in the viral genome. Nevertheless, in spite of these vacuoles, the cells support VACV infection, as viral related structures were seen in these cells. To confirm that PtK2 cells were able to fully sustain virus infection, a virus growth-curve was performed. Cells were infected with MVA-C-ΔF1C(GFP) strain, and the virus production was measured at different times after infection using an immunostaining assay in DF-1 cells (Fig. 1f, g). The kinetics of viral production

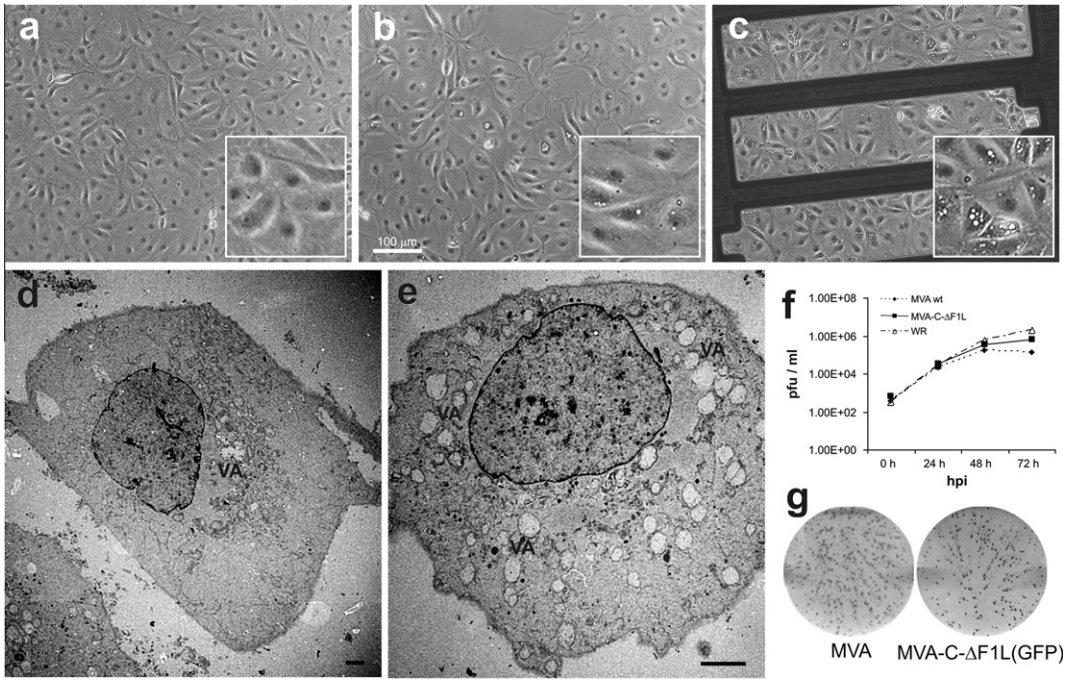


**Fig.1.** Analysis of virus growth of MVA-C-ΔF1L in PtK2 cells on grids. (a) PtK2 cells growing in normal conditions on coverslips visualized by optical phase contrast microscopy. The inset shows a higher magnification of the cells. (b) PtK2 cells growing under FCS deprivation on coverslips visualized by optical phase contrast microscopy. The inset shows a higher magnification of the cells were some vacuoles are visible. (c) Vaccinia virus infected PtK2 cells growing under FCS deprivation on IFR1 Au-grids with a formvar-carbon foil special for X-ray microscopy, visualized by optical phase contrast microscopy. The inset shows a higher magnification of the cells with a significant number of vacuoles in the cytoplasm. (a) and (c) share the same scale bar than (b). (d) TEM image from an epoxy-resin section of an infected cell under standard growth conditions. VA marks the position of some vacuoles. Scale bar represents 1 micron. (e) TEM image of epoxy-resin section of an infected cell under FCS deprivation. VA marks the position of vacuoles within the cytoplasm. Scale bar represents 1 micron. (f) Virus growth curve: Monolayers of PtK2 cells were infected with WR, MVA or MVA-C-ΔF1L at 0.01 PFU/cell. At different times post-infection (0, 24, 48 and 72 h), cells were harvested and virus titers in cell lysates were determined by plaque immunostaining assay in DF-1 cells using rabbit polyclonal antibody against vaccinia virus strain WR. (g) Stained foci in PtK2 cells infected with MVA or MVA-C-ΔF1L after immunostaining assay at 4 days post-infection.

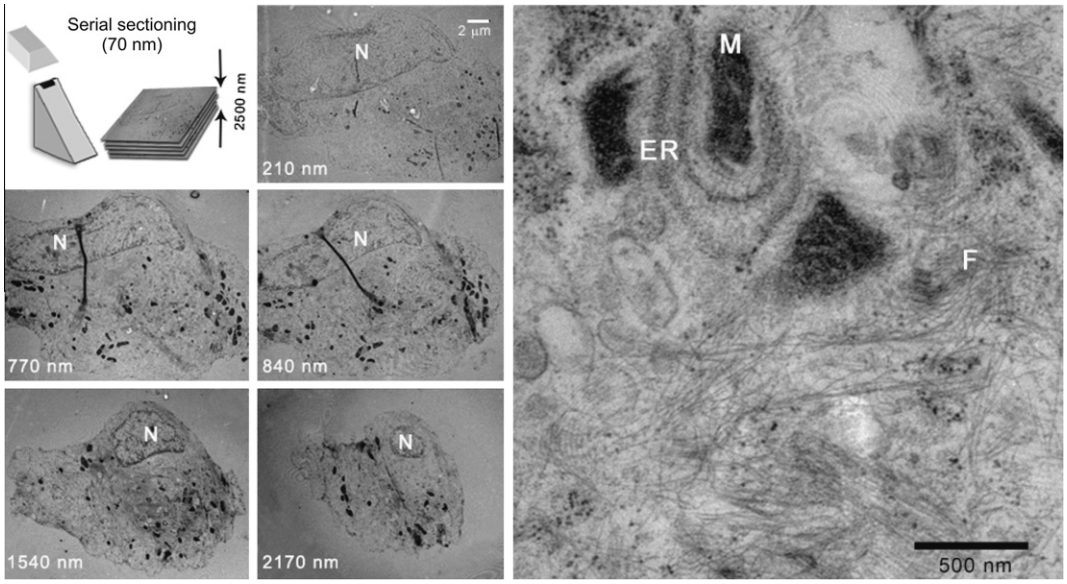


**Fig.2.** TEM analysis of serial sections of infected PtK2 cells fixed by plunge freezing, freeze substituted and embedded in Lowicryl. PtK2 cells grown under FCS deprivation were infected with vaccinia virus and plunge frozen after 18 h post-infection. The samples were freeze-substituted and embedded in Lowicryl resin to collect thin sections following planes parallel to the cell-grid surface. The left panels show different sections of a cell at different heights (labeled in each image). N marks the position of the cell nucleus. The right panel shows a high magnification image of a typical cell revealing good preservation of the cytoplasm. F, ER and M mark the position of filaments, endoplasmic reticulum and mitochondria, respectively.

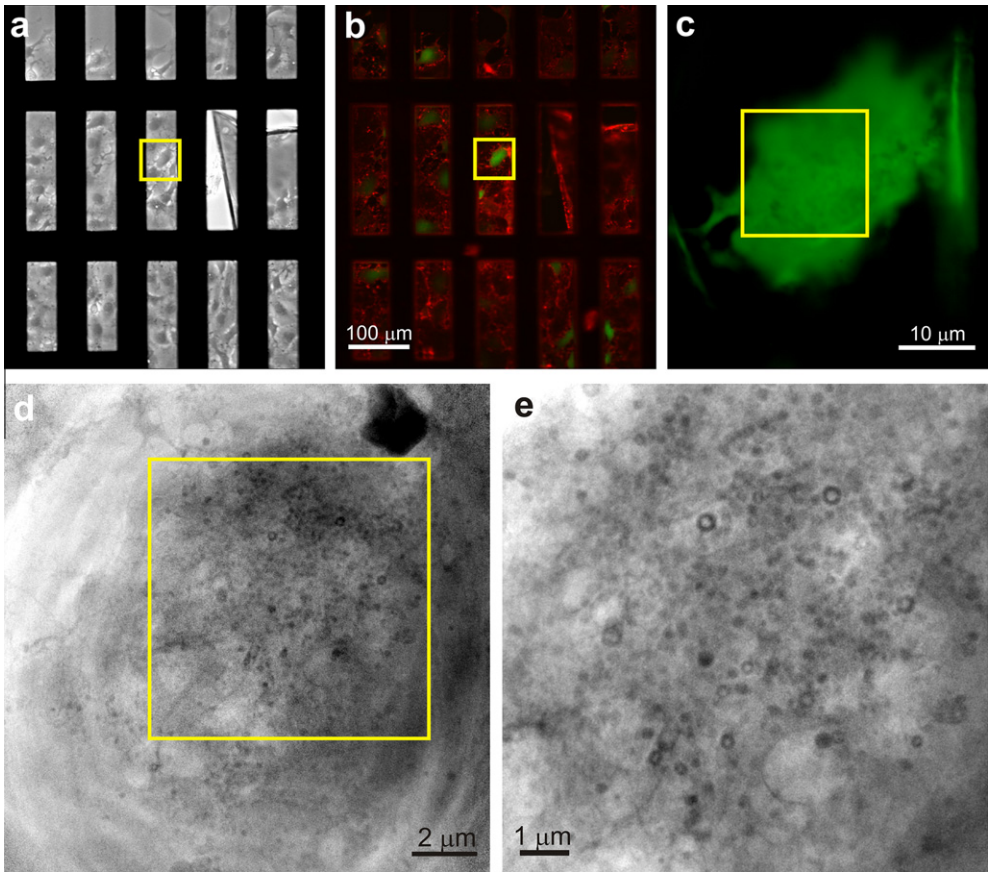


**Fig.3.** Workflow for cryo X-ray nano-tomography data acquisition: From live MVA-C-ΔF1L-GFP infected cells to X-ray projection images. (a) Live optical diffraction interference contrast image of infected cells growing on HZB2 Au-grids over formvar-carbon foil. (b) Live optical fluorescence image of the same area in (a). Cell membranes are red labeled (WGA dye) showing cell boundaries and uninfected cells. In green, viral expression of GFP showing the localization of infected cells. Scale bar represents 100 microns. Magnification is equal in (a) and (b). (c) Cryo-optical fluorescent image (GFP detection) of the same cell enclosed by a yellow square in (a) and (b) collected with the fluorescence microscope integrated in the TXM. (d) Cryo X-ray microscopy projection image (zone plate objective with $dr_n$ = 40 nm, effective pixel size 15.6 nm) of the cell area marked in (c). (e) Cryo X-ray microscopy projection image of the yellow square enclosed area in (d) (zone plate objective with $dr_n$ = 40 nm, effective pixel size 8.6 nm).

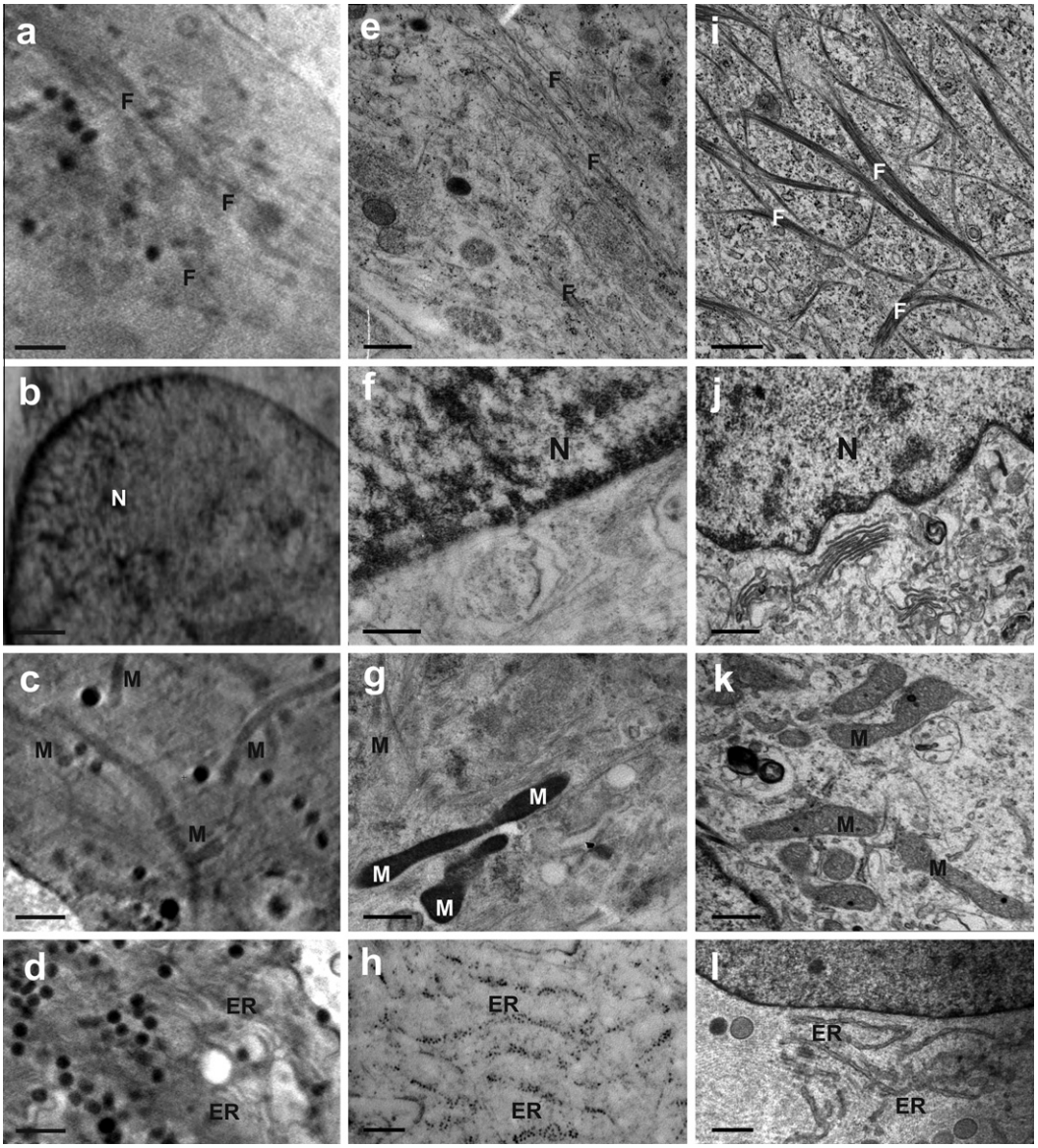


**Fig.4.** Comparison of infected PtK2 cellular ultrastructure by X-ray tomography and TEM freeze substitution and epoxy-resin sectioning. The left panels (a–d) represent planes of the X-ray tomographic reconstructions. The central panels (e–h) are TEM images of sections from freeze-substituted and Lowicryl embedded cells. Right panels (i–l) show TEM images of chemically fixed and contrasted epoxy-resin sections. Upper panels (a, e and f) compare the filaments (F) found in the basal part of the cell. (b, f and j) show the nuclear envelope and chromatin condensations, where N marks the position of the nucleus. (c, g and k) show mitochondria (M). The lower panels (d, h and l) show endoplasmic reticulum (ER). Scale bars represent 0.5 microns.

found for VACV wild type and the two strains (MVA and the GFP containing MVA-C-ΔF1C(GFP)) were identical up to 24 h after infection, although differences in virus titers were observed at 72 h (probably due to the extensive cytopathic effect and the apoptosis events referred above). In addition, the plaque-size morphology between MVA and MVA-C-ΔF1C(GFP) were also similar. The findings of Fig. 1 demonstrate that PtK2 cells infected with MVA-C-ΔF1C(GFP) is a good system to follow virus infection and the assembly cycle.

### 3.2. Fast freezing of PtK2 infected cells

The preservation of the cell ultrastructure is a critical aspect of the sample preparation for tomographic reconstructions. PtK2 cells were grown on the surface of gold microscope grids under serum deprivation, and infected with MVA-C-ΔF1C(GFP). The cells were collected after 18 h post-infection and fast frozen by liquid ethane plunging. The frozen cells were cryo-substituted as described in Section 2, and the samples were sectioned parallel to the substrate plane at different heights to study their preservation level using electron microscopy. Fig. 2 shows the aspect of different sections at increasing distances up to 3 μm towards the interior of the cell from the basal plane in contact with the substrate. The images show a uniform preservation with an overall good preservation of the cell cytoplasm and a reasonable delineation of mitochondria, vacuoles and filamentous structures. These results were consistent among different cells and preparations (up to 8 μm were tested), thus supporting that fast plunging in liquid ethane is a good choice for effective freezing of the relatively thin PtK2 cells.

### 3.3. Detection of areas of interest in infected cell samples

The location of the regions of interest to be imaged is a key issue in X-ray microscopy. To select those cells which were infected by

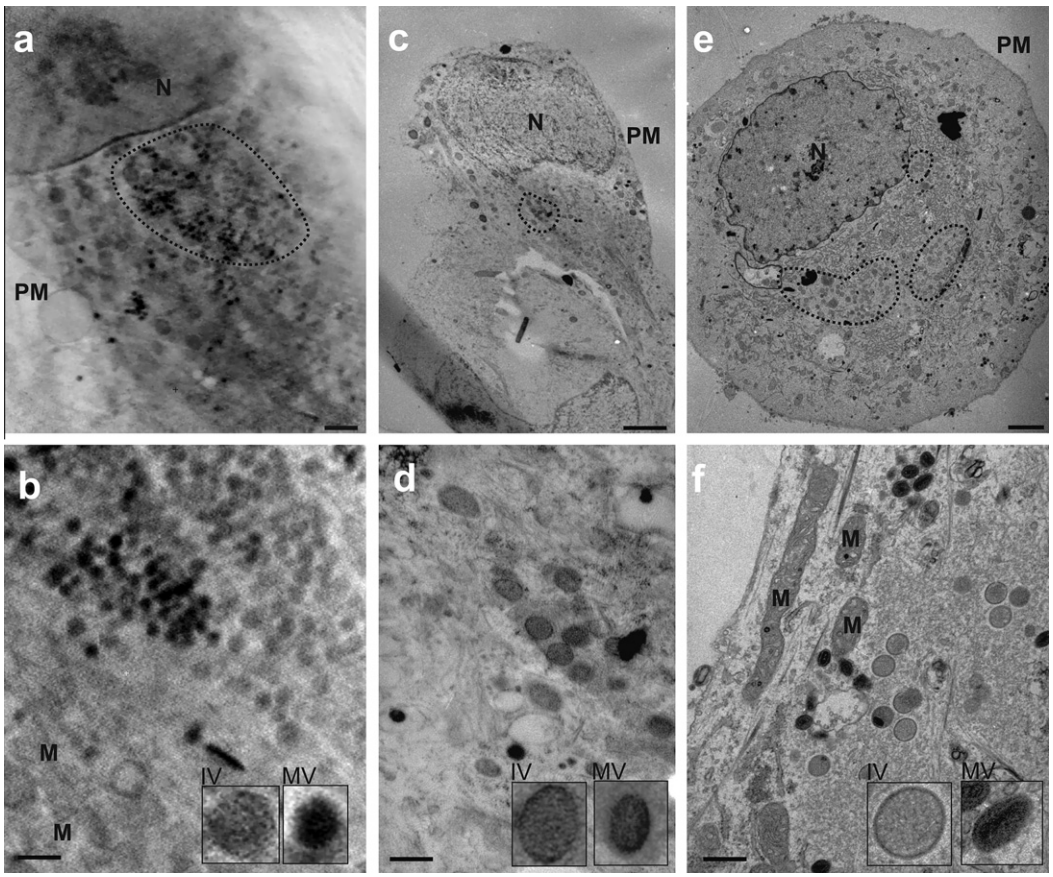


**Fig.5.** Comparison of viral structures in infected PtK2 cells by X-ray tomography and TEM freeze substitution and epoxy-resin sectioning. Left panels (a–b) represent planes of the X-ray tomographic reconstructions. The central panels (c–d) are TEM images of sections from freeze-substituted and Lowicryl embedded cells. Right panels (e–f) show TEM images of chemically fixed and contrasted epoxy-resin sections. Upper panels (a, c and e) compare a cellular overview where it is possible to detect the viral factories, enclosed by doted lines. N and PM mark the position of the nucleus and plasma membrane, respectively. Scale bars represent 2 microns. (b, d and f) are high magnification images of the infected cells cytoplasms where different viral structures are found. The insets in every panel show immature virions (IV) and mature viral particles (MV). M marks the position of mitochondria. Scale bars represent 0.5 microns.

VACV among those cells grown on the surface of the microscope grids that were not infected (Fig. 3a), PtK2 cells were infected with the MVA-C-ΔF1C(GFP) virus strain. This strain expresses the fluorescent protein GFP and, thus, infected cells can be easily detected by "*in vivo*" fluorescence (Fig. 3b). This signal was used to map the position of the infected cells in the framework of the grid marks at room temperature. After freezing, the grids were transferred into the X-ray microscope under liquid nitrogen, and grid marks were used to locate the infected cell coordinates. This location was then cross-checked using the fluorescence microscope integrated in the X-ray microscope, as the GFP signal was clearly visible after plunge freezing (Fig. 3c). Full-field projection images were collected from 10 to 15 μm thick frozen samples containing the infected cells as shown in Fig. 3d. The coordinates of these cell positions were used for collecting cryo X-nano-tomographic data sets (Fig 3d and e).

### *3.4. Comparison of structural features in infected cells by X-ray and electron microscopy*

The selected cell regions following the correlative approach described above were tilted in the X-ray microscope in 1° steps between +65° and −65° using the X-ray microscope goniometer stage. Care was taken to check that after the series acquisition the area did not reveal visual evidences of radiation damage (*i.e.* a 0° projection image before starting the tilt series was compared to a 0° projection image after finishing the tilt series). The series of tilted projection images were aligned and processed as described in Section 2 to yield three-dimensional reconstructed volumes.

The different tomographic reconstructions obtained by cryo X-ray microscopy of PtK2 cells consistently revealed well contrasted volumes, where the main cellular features were immediately evident (Fig. 4a–d). To make a straight identification of these features we performed a systematic comparison of the planes of the X-ray tomographic reconstructions with thin sections imaged by TEM of the same type of samples processed following two procedures. The first one was cryo-substitution and Lowicryl embedding, where the frozen cells were embedded in resin at low temperature, thus minimizing the dehydration induced effects. This preparation method closely mimics the sample cryo-fixation used for X-ray microscopy. The sections obtained from these samples were lightly stained with uranyl acetate to increase the contrast for a better visualization (Fig. 4e–h). The second procedure consists on a more standard chemically fixed embedding in epoxy resin for sectioning. This method has been the classical way to identify virus-related structures due to the high contrast provided by an extensive use of staining reagents (osmium tetroxide, uranyl acetate and lead citrate, see Section 2) (Fig. 4i–l).

Filamentous structures were evident in the basal side of the cell shown in the X-ray tomographic reconstruction (Fig. 4a) resembling those ones found at the same areas by electron microscopy in thin sections after cryo-substitution and uranyl acetate staining (Fig. 4e). The appearance of these structures is similar to actin bundles as recognizable in the fully stained Epoxy-resin embedded

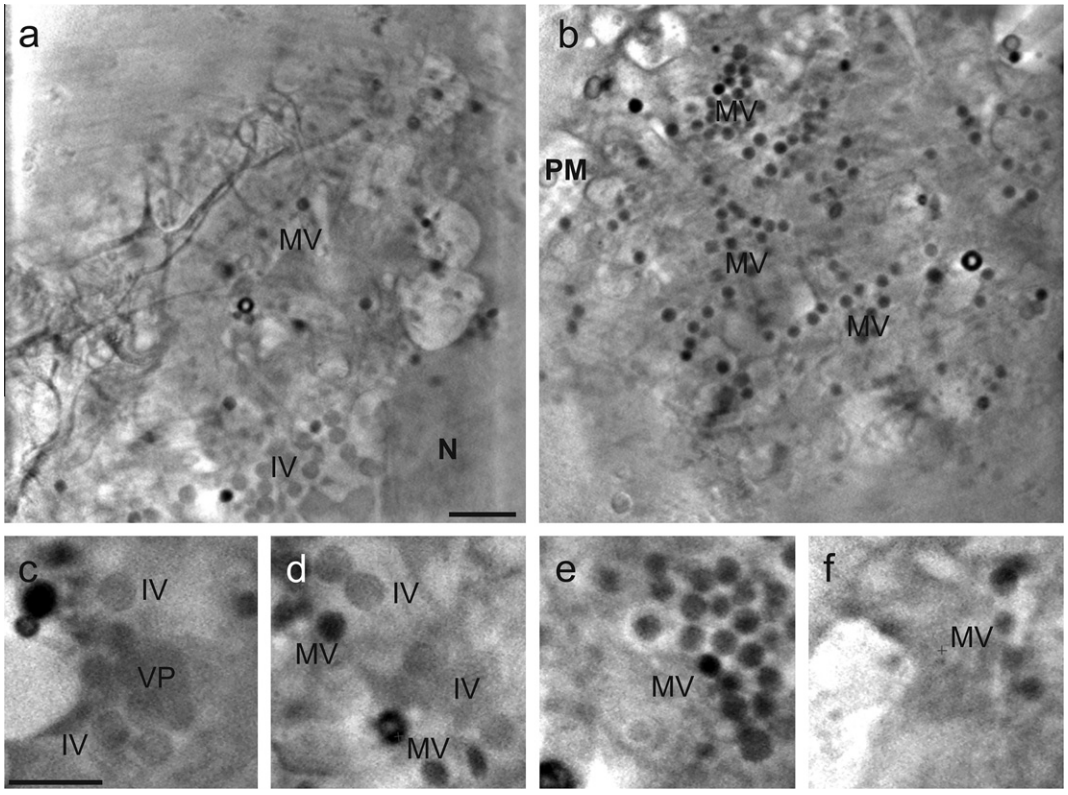


**Fig.6.** Detection of different viral forms in MVA-C-ΔF1L-GFP infected PtK2 cells by cryo X-ray nano-tomography. Panel (a): Basal tomographic plane of a reconstructed cell by cryo X-ray nano-tomography. N marks the position of the nucleus, IV and MV the relative positions of the different immature and mature viral particles, respectively. Scale bar represents 1 micron. (b) Upper tomographic plane of the same reconstruction as in (a). PM marks the position of the plasma membrane of the cell and MV points to the mature viral particles. The scale is the same as in (a). (c) Formation of immature virions (IV) from viroplasm and crescents (VP). Scale bar represents 0.5 microns. (d) Area of the cytoplasm showing immature particles (IV) close to mature virions (MV). (e) A group of densely packaged mature particles (MV). (f) Mature particles near the plasma membrane (PM) of the cell. Panels (c)–(d) have the same magnification.

samples (Fig. 4i). The nucleus is especially well contrasted in the cryo X-ray tomograms (Fig. 4b). Different chromatin aggregates are visible, as well as the nuclear envelope. The comparison with the stained Lowicryl (Fig. 4f), and Epon sections (Fig. 4j) reveals that the unstained X-ray tomograms offer at this magnification as much overall structural features as the conventional electron microscopy images. The mitochondria in infected PtK2 cells appear elongated with characteristic shapes in the electron microscope images from thin sections of Epon and Lowicryl embedded material (Fig. 4k and g, respectively). The same type of images can be found in the X-ray tomographic reconstructions (Fig. 4c). Other cellular features, as the endoplasmic reticulum (ER) are more difficult to visualize unless a full staining method is applied (Fig. 4l). In cryo-substituted Lowicryl sections the ER is hardly seen (Fig. 4h), similar to the appearance of certain areas in the X-ray tomographic reconstructions (Fig. 4d).

### *3.5. Detection of VACV particles in infected cells by cryo X-ray nano-tomography*

The X-ray tomograms of VACV infected PtK2 cells showed the presence of certain areas of the cytoplasm with characteristic features resembling the well documented vaccinia factories. These cytoplasmic regions are heavily modified by a high concentration of viral components that exclude cell organelles and membranes. These areas are frequently surrounded by filaments and mitochondria (Condit et al., 2006; Risco et al., 2002). Fig. 5a shows a panoramic plane from an X-ray tomographic reconstruction, where there is a region near the nucleus that presents a distinct aspect respect to other cytoplasmic areas. This type of area has not been seen in X-ray tomograms from uninfected cells, and it resembles genuine viral factories that are also found by electron microscopy of thin sections of cryo-substituted PtK2 infected cells embedded in Lowicryl (Fig. 5c), and in fully stained sections processed for Epoxy-resin embedding (Fig. 5e).

Higher magnification images obtained near the viral factory-like regions in the X-ray tomographic reconstructions (with an estimated 3D-resolution up to 55 nm), show the presence of two types of particles, which differ in their shape and size: one is more rounded (diameter around 350 nm) and it encloses a medium density material, while the other is smaller (diameter around 250 nm) and much more dense, as it appears darker (Fig. 5b, insets). The overall characteristics of these particles are similar to the standard views of the two main VACV assembly intermediate particles (immature virus, IV, and internal mature virus, MV), as defined by electron microscopy of cryo-substituted infected cell Lowicryl sections (Fig. 5d), and Epon stained sections (Fig. 5f).

Planes along the X-ray tomographic reconstructions reveal a compartmentalization of the different viral particles: the IVs aggregated in areas near the nuclei (Fig. 6a), while MVs are grouped towards the cell periphery (Fig. 6b). Closer examination of the viral factories and the viral-related particles in their neighborhood reveals the presence of viroplasm coupled to crescent-like and incomplete IVs (Fig. 6c). In the periphery of these areas there is an accumulation of IVs that delineate a transition zone towards the areas where MVs accumulate (Figs. 6b, 5b). The appearance of the intracellular particles associated to MVs within the cell cytoplasm (Fig. 6e, f) is similar to the tomographic reconstructions obtained for the isolated, ice embedded VACV using cryo X-ray nano-tomography (Carrascosa et al., 2009).

### 3.6. Analysis of the radiation damage induced during X-ray tomographic data acquisition

Acquisition of images during X-ray microscopy, even under cryogenic conditions, involves the exposure of the sample to radiation, thus generating chemical and physical damages to it. The average irradiation for the acquisition of an image in the HZB X-ray microscope used in these experiments (beamline U41 at BESSY II, $5 \times 10^8$ photons/$\mu m^2$ at 510 eV) might be estimated to around $5 \times 10^7$ Gy per image, which amounts up to around $5 \times 10^9$ Gy for the collection of a complete tomography data set. Although the radiation damage problem has been thoroughly studied in electron cryo-microscopy, much less detailed measurements exist in the case of X-ray microscopy. To get an insight into how this radiation level might affect the structural information retrieved by X-ray microscopy at the magnification and resolution attainable in these experiments, we compared the ultrastructure of samples obtained before and after X-ray irradiation using electron microscopy of thin sections from these samples.

To this end, we collected the frozen X-ray irradiated grids which were used for the tomographic data acquisition described above. The specific marks on the HZB2 grids allowed us to identify those areas were tilt series were acquired (heavily irradiated) from those areas which suffered only marginal irradiation during the screening procedure. The grids were kept under liquid nitrogen and subsequently they were freeze-substituted and plastic embedded as described in Section 2. The areas were selected using the grid features (related to the regions of interest defined by the correlative microscopy described above), and then serial ultrathin sections were produced and processed for observation by electron microscopy (Fig 7). The overall ultrastructure of cells in the irradiated areas (Fig. 7c) did not show significant differences to those cells in non-irradiated areas (Fig. 7a). Although the sections derived from heavily irradiated areas showed a slightly faster staining than the non-irradiated ones, in both cases the cytoplasmic aspect, as well as the definition of the different organelles are undistinguishable (Fig. 7b, d). Furthermore, the two types of viral-related particles (IVs and MVs) showed identical features, including their outer envelopes and viroplasm density (Fig. 7b, d; insets).

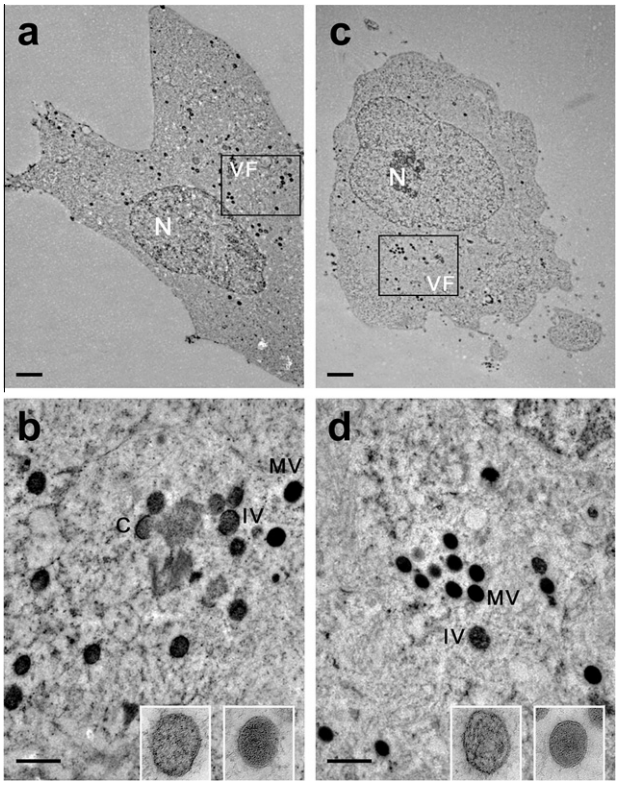


**Fig.7.** Ultrastructure comparison after X-ray irradiation. HZB2 grids used for cryo X-ray tomography were subjected to freeze-substitution and embedding in Lowicryl resin. Areas containing irradiated and non-irradiated cells were identified based on grid marks and features. Thin sections were obtained by ultramicrotomy and observed by electron microscopy. (a) .Cell section from a non-irradiated area. N marks the position of the nucleus, VF marks a viral factory. Scale bar represents 2 microns. (b) Higher magnification detail of the cytoplasm from (a). C shows a viral crescent, IV immature virus and MV mature virus. The left inset shows a magnified view of an IV, and the right inset a MV. Scale bar represents 500 nm. (c) Section of a heavily X-ray irradiated cell used to collect two full X-ray tomographic data sets. N marks the position of the nucleus, VF marks a viral factory. The scale is the same as in (a). (d) Higher magnification detail of the cytoplasm from (c). IV shows immature virus and MV mature virus. The left inset shows a magnified view of an IV, and the right inset a MV. Scale bar represents 500 nm.

## 4. Discussion

The incorporation of X-ray microscopy to the analysis of biological materials is based on the possibility to penetrate large cellular volumes (up to 10 μm) to retrieve chemical and structural information at resolutions intermediate between light and electron microscopy. The combination of methods based on cryogenic sample preparation and image acquisition at low temperatures has led to the three-dimensional reconstruction of frozen cells revealing their internal structures (Hanssen et al., 2010; Larabell and Le Gros, 2003; Schneider et al., 2010; Weiss et al., 2000). Here we have studied the structure of cells infected with VACV in an attempt to get clues on the possibility to detect relatively small structural features within the whole cell cytoplasm. Although purified vaccinia virus particles were seen by cryo X-ray tomography without any fixative or staining (Carrascosa et al., 2009), their detection within the crowded cellular cytoplasm was not evident. The combination of light, electron and X-ray microscopy allows following different cellular features at complementary 3D resolution levels without using any fixative or contrasting reagent. To correlate the different microscopy methods we used a fluorescent probe associated to the expression of GFP by an engineered strain of VACV. Regions of interest were detected by means of the fluorescence characteristic of the infected cells, which were observed in the fluorescent light microscope at room temperature as well as after freezing the cells, allowing us to identify the relevant cells under the X-ray microscope using grid coordinates marks.

The cryo X-ray nano-tomograms from VACV infected cells showed a number of well preserved cellular organelles, whose structures were readily recognizable by comparison to the corresponding thin sections of equivalent samples subjected to chemical fixation and staining imaged by electron microscopy. The resolution level attained in our cryo X-ray tomograms is such that it has been possible to detect cytoplasmic regions modified by the viral infection (viral factories), as well as two distinct types of viral particles, the IVs and the MVs. The morphological features shown in the frozen, unstained samples reconstructed from X-ray tomograms are comparable, albeit at a slightly lower resolution, to the structures described by electron microscopy of thin sections of chemically fixed and stained material. However, the main difference between these electron and X-ray microscopy results is that the former correspond to 70 nm sections of the cell, while the later derive from whole 10 to 12 μm thick cells, thus avoiding the biased interpretation derived from the analyses of partial cellular volumes, and opening the way to quantitative studies of the viral infection process at improved resolutions, including also the macromolecular events associated to the cytopathic effects produced in the course of virus infections.

A main drawback in electron and X-ray microscopy is radiation damage. The use of cryogenic temperatures lowers the damage, but it is a main limiting factor for these microscopy methods that has to be minimized using as low dosages as possible to collect useful information (Knapek and Dubochet, 1980). We have done a preliminary estimation of the effect of X-ray irradiation during tomographic data collection by comparison of the ultrastructure observed by electron microscopy from thin sections of infected cells derived either from X-ray irradiated or non-irradiated material. By collecting the samples after X-ray tomography, and using the marks on the HZB2 microscope grid to identify those cells which were irradiated during tomographic tilt series, we embedded those areas in resin for thin sectioning and observation under the electron microscope. The ultrastructure revealed by electron microscopy showed an overall similar aspect of the cytoplasmic background, while the main structural features of the cell organelles remained basically similar to those seen in non-irradiated areas. Even the structural details characteristic of the two types of viral-related particles (IVs and MVs) were identical with and without X-ray irradiation. Our results show for the first time that the irradiated areas preserve most of the ultrastructure as defined at the thin section electron microscopy level. Further detailed analysis will be required in the future to fully understand the effect of X-ray radiation damage during cryo X-ray imaging at improved resolutions.

## Acknowledgments

This work was supported by Grants BFU2008-2328, BFU2011-29038 and Consolider CSD2007-00010 from the MICINN, and S009/MAT-1507 from the CM (to J.L.C) and SAF.2008-02036 (to M.E.). The X-ray microscopy work was funded partly by the Human Frontier Science Program (HFSP) Research Grant Ref. RGP0053/2005-C, and by the European Community's Seventh Framework Programme (FP712007-2013) under grant agreement n° 226716. Fluorescence microscopy was done in the CNB confocal microscopy Service. We acknowledge the gift of PtK2 cells by Dr. I. Barasoain. M.C. is a fellow of La Caixa/CNB International PhD Program.

## Appendix A. Supplementary data

Supplementary data associated with this article can be found, in the online version, at doi:10.1016/j.jsb.2011.12.001.

## References

Agulleiro, J.I., Fernandez, J.J., 2011. Fast tomographic reconstruction on multicore computers. Bioinformatics 27, 582–583.
Baumeister, W., Steven, A.C., 2000. Macromolecular electron microscopy in the era of structural genomics. Trends Biochem. Sci. 25, 624–631.
Carrascosa, J.L., Chichon, F.J., Pereiro, E., Rodriguez, M.J., Fernandez, J.J., Esteban, M., Heim, S., Guttmann, P., Schneider, G., 2009. Cryo-X-ray tomography of vaccinia virus membranes and inner compartments. J. Struct. Biol. 168, 234–239.
Condit, R.C., Moussatche, N., Traktman, P., 2006. In a nutshell: structure and assembly of the vaccinia virion. Adv. Virus Res. 66, 31–124.
Cyrklaff, M., Risco, C., Fernandez, J.J., Jimenez, M.V., Esteban, M., Baumeister, W., Carrascosa, J.L., 2005. Cryo-electron tomography of vaccinia virus. Proc. Natl Acad. Sci. USA 102, 2772–2777.
Cyrklaff, M., Linaroudis, A., Boicu, M., Chlanda, P., Baumeister, W., Griffiths, G., Krijnse-Locker, J., 2007. Whole cell cryo-electron tomography reveals distinct disassembly intermediates of vaccinia virus. PLoS ONE 2, e420.
Chao, W., Harteneck, B.D., Liddle, J.A., Anderson, E.H., Attwood, D.T., 2005. Soft X-ray microscopy at a spatial resolution better than 15 nm. Nature 435, 1210–1213.
Chichon, F.J., Rodriguez, M.J., Risco, C., Fraile-Ramos, A., Fernandez, J.J., Esteban, M., Carrascosa, J.L., 2009. Membrane remodelling during vaccinia virus morphogenesis. Biol. Cell 101, 401–414.
Fernandez, J.J., 2009. TOMOBFLOW: Feature-preserving noise filtering for electron tomography. BMC Bioinf. 10, 178.
Flint, S.J., Enquist, L.W., 2009. A.S.f. Microbiology. In: Racaniello, V.R., Skalka, A.M. (Eds.), Principles of Virology: Foundations. ASM Press.
Galbraith, C.G., Galbraith, J.A., 2011. Super-resolution microscopy at a glance. J. Cell Sci. 124, 1607–1611.
Hanssen, E., Knoechel, C., Klonis, N., Abu-Bakar, N., Deed, S., LeGros, M., Larabell, C., Tilley, L., 2010. Cryo transmission X-ray imaging of the malaria parasite, *P. falciparum*. J. Struct. Biol. 173, 161–168.
Hunter, E., 2007. Virus assembly. In: Knipe, D.N., Howley, P.M. (Eds.), Fields Virology. Lippincott Williams & Wilkins, a Wolters Klumber Business, Philadelphia, pp. 141–168.
Jones, S.A., Shim, S.H., He, J., Zhuang, X., 2011. Fast, three-dimensional super-resolution imaging of live cells. Nat. Methods 8, 499–505.
Kirz, J., Rarback, H., 1985. Soft X-ray microscopes and their biological applications. Rev. Sci. Instrum. 56, 1–13.
Knapek, E., Dubochet, J., 1980. Beam damage to organic material is considerably reduced in cryo-electron microscopy. J. Mol. Biol. 141, 147–161.
Kremer, J.R., Mastronarde, D.N., McIntosh, J.R., 1996. Computer visualization of three-dimensional image data using IMOD. J. Struct. Biol. 116, 71–76.
Larabell, C.A., Le Gros, M.A., 2003. X-ray tomography generates 3-D reconstructions of the yeast, *Saccharomyces cerevisiae*, at 60 nm resolution. Mol. Biol. Cell.
Larabell, C.A., Nugent, K.A., 2010. Imaging cellular architecture with X-rays. Curr. Opin. Struct. Biol. 20, 623–631.
Lucic, V., Forster, F., Baumeister, W., 2005. Structural studies by electron tomography: from cells to molecules. Annu. Rev. Biochem. 74, 833–865.
Marabini, R., Masegosa, I.M., San Martin, M.C., Marco, S., Fernandez, J.J., de la Fraga, L.G., Vaquerizo, C., Carazo, J.M., 1996. Xmipp: an image processing package for electron microscopy. J. Struct. Biol. 116, 237–240.
Martone, M.E., Zhang, S., Gupta, A., Qian, X., He, H., Price, D.L., Wong, M., Santini, S., Ellisman, M.H., 2003. The cell-centered database: a database for multiscale structural and protein localization data from light and electron microscopy. Neuroinformatics 1, 379–395.
Moss, B., 2007. Poxviridae: the viruses and their replication, p. 2905–2975. In: Knipe, D.N., Howley, P.M. (Eds.), Field's Virology. Lippincott Williams and Wilkins, Philadelphia, pp. 2905–2975.
Pettersen, E.F., Goddard, T.D., Huang, C.C., Couch, G.S., Greenblatt, D.M., Meng, E.C., Ferrin, T.E., 2004. UCSF Chimera – a visualization system for exploratory research and analysis. J. Comput. Chem. 25, 1605–1612.
Pierson, J., Fernandez, J.J., Bos, E., Amini, S., Gnaegi, H., Vos, M., Bel, B., Adolfsen, F., Carrascosa, J.L., Peters, P.J., 2010. Improving the technique of vitreous cryo-sectioning for cryo-electron tomography: electrostatic charging for section attachment and implementation of an anti-contamination glove box. J. Struct. Biol. 169, 219–225.
Rehbein, S., Heim, S., Guttmann, P., Werner, S., Schneider, G., 2009. Ultrahigh-resolution soft-X-ray microscopy with zone plates in high orders of diffraction. Phys. Rev. Lett. 103, 110801.
Rigort, A., Bauerlein, F.J., Leis, A., Gruska, M., Hoffmann, C., Laugks, T., Bohm, U., Eibauer, M., Gnaegi, H., Baumeister, W., Plitzko, J.M., 2010. Micromachining tools and correlative approaches for cellular cryo-electron tomography. J. Struct. Biol. 172, 169–179.
Risco, C., Rodriguez, J.R., Lopez-Iglesias, C., Carrascosa, J.L., Esteban, M., Rodriguez, D., 2002. Endoplasmic reticulum–Golgi intermediate compartment membranes and vimentin filaments participate in vaccinia virus assembly. J. Virol. 76, 1839–1855.
Rodriguez, D., Barcena, M., Mobius, W., Schleich, S., Esteban, M., Geerts, W.J., Koster, A.J., Griffiths, G., Locker, J.K., 2006. A vaccinia virus lacking A10L: viral core proteins accumulate on structures derived from the endoplasmic reticulum. Cell. Microbiol. 8, 427–437.
Scheres, S.H., Nunez-Ramirez, R., Sorzano, C.O., Carazo, J.M., Marabini, R., 2008. Image processing for electron microscopy single-particle analysis using XMIPP. Nat. Protoc. 3, 977–990.
Schneider, G., 1998. Cryo X-ray microscopy with high spatial resolution in amplitude and phase contrast. Ultramicroscopy 75, 85–104.
Schneider, G., Schliebe, T., Aschoff, H., 1995. Cross-linked polymers for nanofabrication of high-resolution zone plates in nickel and germanium. J. Vac. Sci. Technol., B: Microelectron. Nanometer Struct. 13, 2809–2812.
Schneider, G., Anderson, E., Vogt, S., Knochel, C., Weiss, D., Legros, M., Larabell, C., 2002. Computed tomography of cryogenic cells. Surf. Rev. Lett. 9, 177–183.
Schneider, G., Denbeaux, G., Anderson, E., Pearson, A., Bates, W., Vogt, S., Knochel, C., Meyer, M.A., Zschech, E., 2003. High resolution X-ray tomography with applications in biology and materials science. J. Phys. IV 104, 607–613.
Schneider, G., Guttmann, P., Heim, S., Rehbein, S., Mueller, F., Nagashima, K., Heymann, J.B., Muller, W.G., McNally, J.G., 2010. Three-dimensional cellular ultrastructure resolved by X-ray microscopy. Nat. Methods 7, 985–987.
Sorzano, C.O., Marabini, R., Velazquez-Muriel, J., Bilbao-Castro, J.R., Scheres, S.H., Carazo, J.M., Pascual-Montano, A., 2004. XMIPP: a new generation of an open-source image processing package for electron microscopy. J. Struct. Biol. 148, 194–204.
Weiss, D., Schneider, G., Niemann, B., Guttmann, P., Rudolph, D., Schmahl, G., 2000. Computed tomography of cryogenic biological specimens based on X-ray microscopic images. Ultramicroscopy 84, 185–197.